CHAPTER 3

Synthesis and photocatalytic application of magnetically recyclable starch functionalized $Fe_3O_4/Ag/Ag_2O$ nanostructures

3.1 Introduction

Hydrogen peroxide (H_2O_2) is a potent green oxidizing agent [Sato *et al.* (1998), Compos- Martin *et al.* (2006)] widely used in various advanced oxidation processes and organic syntheses [Shaegh *et al.* (2012)]. Currently, the commercial production of H_2O_2 is by the anthraquinone process [Sandelin *et al.* (2003)]. The process involves complex sequential hydrogenation and oxidation of anthraquinones in organic solvents, requiring a significant amount of energy, chemicals and is accompanied by waste generation as well. Additionally, the processes of transport, handling, and storage of bulk quantities of H_2O_2 are unsafe and not economical. Consequently, efforts have been made in recent years for in-situ onsite production of H_2O_2. While a direct reaction between H_2 and O_2 can produce H_2O_2, this requires expensive catalysts with a high risk of explosion [Lunsford *et al.* (2003), London *et al.* (2003), Edwards *et al.* (2005), Voloshin *et al.* (2007)].

A viable approach to this problem is the photocatalytic production of H_2O_2 over semiconducting materials. Initial studies in this area saw the use of TiO_2 in conjunction with electron donors like alcohol [Kormann *et al.* (1988), Goto *et al.* (2004), Hirakawa *et al.* (2008), Shiraishi *et al.* (2013)]. Subsequent research showed that H_2O_2 formation occurred at an increased rate when co-catalyst was Ag or Au. In particular, Ag/TiO_2 exhibited better photocatalytic H_2O_2 production results [Tsukamoto *et al.* (2012)] with the plasmonic Ag metal co-catalyst generating excited hot electrons with enough redox potentials to reduce oxygen [Wen *et al.* (2017a), Wen *et al.* (2017b)]. However, wide-bandgap semiconductors (like TiO_2) cannot utilize visible light and require an organic electron donor to sustain the process.

Environmentally friendly, sustainable H_2O_2 production requires visible light photocatalytic oxidation of water without any additional electron donating agent. For

this to happen, efficient water oxidation is needed to sustain the photocatalytic process alongside two-electron oxygen reduction for H_2O_2 formation. The prevention of byproducts and further purification steps are the main advantages [Shiraishi *et al.* (2014), Zhang *et al.* (2016), Thakur *et al.* (2017)]. Perhaps the first photocatalytic H_2O_2 production report without any organic electron donor molecule was on composites of TiO_2/rGO (reduced graphene oxide). But this was again a photocatalyst requiring UV light. Recent research reports have demonstrated visible light H_2O_2 production on composites of noble metal nanoparticles (as co-catalysts) and suitable visible range semiconductors [Hirakawa *et al.* (2016)]. Other researchers have also shown visible light H_2O_2 formation on nanocomposites of suitable small bandgap semiconductors (like CdS) with electron-conducting supports like reduced graphene oxides [Thakur *et al.* (2017)]. Authors of another recent publication reported H_2O_2 generation on plasmonic Ag graphene-Cu nano-sandwich catalysts [Liu *et al.* (2018)] by efficient utilization of noble metal hot electrons. These investigators demonstrated that plasmonic hot electrons of Ag could reduce oxygen by the two-electron pathway for the specific formation of H_2O_2.

The separation and reuse of powdered semiconductor photocatalysts are quite problematic and costly. Two main issues owing to this are the loss of the photocatalyst and secondary pollution due to its particles. An economical solution to these problems is the fabrication of superparamagnetic nanoparticles as photocatalysts for various applications [Lv *et al.* (2016), Tang *et al.* (2019), Shao *et al.* (2019), Tang *et al.* (2020)]. The application of an external magnetic field magnetizes superparamagnetic nanoparticles. Such nanoparticles become de-magnetized after the removal of the magnetic field. Sonication can re-disperse the nanoparticles for efficient reuse. Likewise, the photocatalysts for H_2O_2 preparation should also be magnetically

recyclable for extensive use in research laboratories and industries. However, to the best of our knowledge, there is no publication on magnetically reusable H_2O_2 production photocatalysts. Hence, the fabrication of a visible light superparamagnetic photocatalyst, which can produce H_2O_2 at a significant rate from water and oxygen only, is a topical research problem [Zuo *et al.* (1992), Zheng *et al.* (2016)].

The above discussion motivated us to investigate the photocatalytic ability of superparamagnetic starch functionalized $Fe_3O_4/Ag/Ag_2O$ (s-$Fe_3O_4/Ag/Ag_2O$) nanocomposites to efficiently produce H_2O_2 from only water and oxygen under visible light irradiation. The following are the reasons for the choice of the composition of this nanocomposite. Magnetite nanoparticles stabilized by different organic modifiers like dextrin, citrate, etc. possess band gaps over 2.1 eV [Radoń *et al.* (2017)]. Starch stabilized magnetite nanoparticles (SMNPs) also show similar bandgap with excellent water dispersibility. Besides this, the investigated photocatalyst consists of components capable of water oxidation and oxygen reduction (along with proper oxygen adsorption properties). Magnetite and Ag have superior O_2 adsorption properties, and as mentioned earlier, the latter is also known for its two-electron oxygen reduction properties [Liu *et al.* (2018), Takei *et al.* (2010), Zhou *et al.* (2018)].

In the present chapter, s-$Fe_3O_4/Ag/Ag_2O$ nanocomposites were prepared by a step-wise co-precipitation protocol. XRD, TEM, and XPS techniques were used to find various aspects of these nanoparticles. UV-DRS and Mott-Schottky (MS) were employed to determine the bandgaps and the band positions of the different components of the composite nanoparticles. The analysis showed that the formation of fine p-type Ag_2O nanostructures smaller than their quantum confinement regimes on the SMNP cores increased their direct bandgaps to more than 1.4 eV [Xu *et al.* (2000), Li *et al.* (2015), Smith *et al.* (2010)]. Also, the precipitation of fine Ag_2O nanostructures on n-

type SMNPs results in nanocomposites with staggered band alignment of the component phases. The p-n heterojunction lowers the valence band (VB) position of magnetite. The final section proposes a plausible mechanism to explain the observed H_2O_2 formation properties.

3.2 Experimental

3.2.1 Preparation of starch functionalized magnetite nanoparticles

Synthesis of starch functionalized superparamagnetic magnetite nanoparticles (SMNPs) was carried out as described elsewhere [Singh *et al.* (2016)]. Materials used in the synthesis of SMNPs were analytical grade iron (II) sulfate heptahydrate (Merck), NaOH (Merck), and starch. An aqueous solution of appropriate amounts of iron (II) sulfate heptahydrate and starch was added drop-wise into a previously heated 0.4 M NaOH (Merck) solution. Throughout the process, the overall reaction temperature of the reaction mixture was maintained at 80 ^oC. After completing the addition, the whole reaction mixture was heated at 80 ^oC for two more hours until the formation of a dark black precipitate. The precipitate obtained was separated by magnetic decantation, repeatedly washed until neutral, and then dried at 40 ^oC in a hot air oven.

3.2.2 Synthesis of Fe_3O_4/ Ag /Ag_2O nanocomposite

A suspension of re-dispersed 38 mg of SMNPs (in 40 ml of water) and 20 ml of 0.01 M $AgNO_3$ (Merck) were mixed in a conical flask. The stoppered conical flask was then agitated on a water bath shaker for 24 hours (for ensuring adsorption equilibrium). This suspension was then added in a drop-wise manner to 40 mL of 0.15 M NaOH with constant heating and stirring. The reaction mixture thus obtained was heated at 60 ^oC with stirring for two more hours. The prepared nanocomposite precipitate was magnetically separated and washed several times with distilled water until the washings

turned neutral. Finally, the precipitate washing was by ethanol. The as-prepared nanocomposite (C1) was dried (at 40°C) in a hot air oven. The same protocol fabricated the second nanocomposite sample (C2) but with a double AgNO3 concentration.

3.2.3 Photocatalytic Activity

Firstly 3 mg catalyst was dispersed in 10 mL water by ultrasonication for 20 min. 400 µL of this catalyst suspension was then added to 4 mL of water at pH 3 (adjusted with the help of 0.1 M HCl) in a 10 mL flask. The reaction mixture was kept in the photocatalytic chamber under cool white LED with visible light radiation of incident power 0.1470 watts/cm^2.

3.2.4 Hydrogen peroxide determination

The amount of H_2O_2 generated was determined by redox titration with $KMnO_4$ (0.2 mM) acidified by 1 M H_2SO_4. The photocatalyst in the aqueous suspension was magnetically separated after a one-hour exposure to visible light. The aqueous solution obtained after the removal of the superparamagnetic nanoparticles was titrated against acidified $KMnO_4$ solution. Color change to pink indicated the endpoint, where the concentration of the $KMnO_4$ solution was considered to be equivalent to the concentration of H_2O_2.

3.2.5 Analysis

UV-visible absorption spectra measurements of Fe_3O_4/Ag/Ag_2O aqueous dispersions were on Agilent Cary 60 spectrophotometer. Rigaku Miniflex 600 instrument determined the X-ray diffraction patterns of the samples. The TEM imaging of the Fe_3O_4@Ag/Ag_2O samples was carried out with FEI Technai-20 G2 operating at a voltage of 200 kV. The solid-state UV-visible measurement was performed on the Shimadzu Pharmaspec UV-1700 model, working in the 200−800 nm spectral range.

X-ray photoelectron spectroscopy (XPS) was carried out on ESCA M-Probe (Al Kα rays λ = 8.33 Å). Survey scans were performed with a detector pass energy of 158.9 eV; high-resolution spectra were recorded with a pass energy of 22.9 eV. All spectra were referenced to adventitious carbon signal at 284.8 eV and fitted using DS (0.0001,400) line shape for elemental Ag metal peaks as well as GL (30) line shape for all other peaks with Casa XPS software from Casa Software Ltd. The electrochemical analysis was done on CH instrument model CHI-7044.

3.3 Results and discussion

3.3.1 Characterization

Figure 3.1 shows the UV-visible spectra of the two aqueous dispersions of nanoparticles prepared in this study. Both samples of nanoparticles (C1 and C2) display broadened featureless absorbance curves. There is a small maximum at about 390 nm in the UV-visible spectrum of C1 but with considerable broadening. On the other hand, the spectrum of C2 exhibits a maximum absorbance from 390 to about 500 nm range of wavelength. While such broad absorbance spectra are characteristic of Ag_2O aqueous dispersions [Wang *et al.* (2011), Yang *et al.* (2016)], the formation of some elemental silver is also possible.

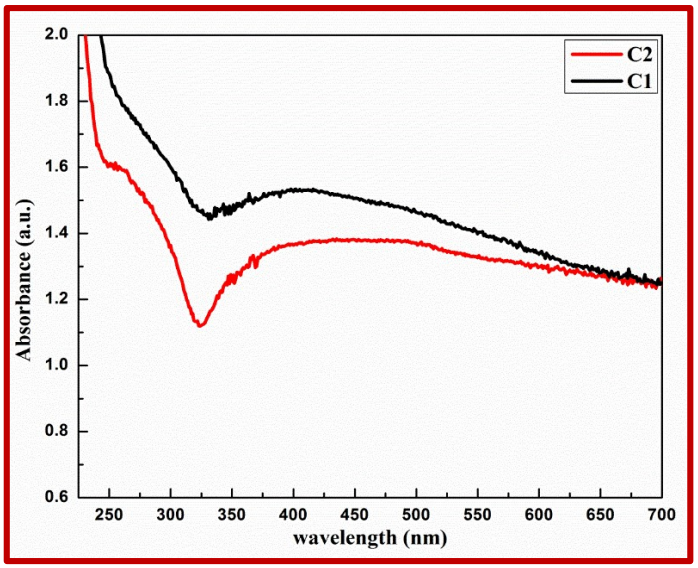

Figure 3.1 UV-Vis absorbance spectra of aqueous C1 and C2 dispersion.

Phases formed were identified by the X-ray diffraction analysis of powder samples of C1, C2, and SMNPs (Figure 3.2). The XRD peaks of the powder samples C1 and C2 could be indexed to magnetite (JCPDS89-2355), Ag_2O (JCPDS75-1532) and FCC Ag (JCPDS87-0717) phases. The peaks at 44.2°, 64.3°, and 77.3° 2θ values correspond to the FCC Ag phase. The strongest peak at 38.1° can be indexed to both FCC Ag (111) and the (200) planes of Ag_2O. Since, the d-values of Ag (111) plane and the (200) plane of Ag_2O are quite close (2.359 Å for Ag_2O and 2.358 Å for Ag), therefore, it is not possible to distinguish between two planes. Clearly, besides magnetite, both reduced FCC Ag and Ag_2O phases have been formed in C1 and C2. As mentioned earlier, SMNPs was the primary starting precursor for the preparation of both C1 and C2. Since starch is known to get partially hydrolyzed under alkaline conditions, [Taylor *et al.* (1993)] the glucose generated from such hydrolysis seemed to be responsible for the formation of a reduced Ag phase.

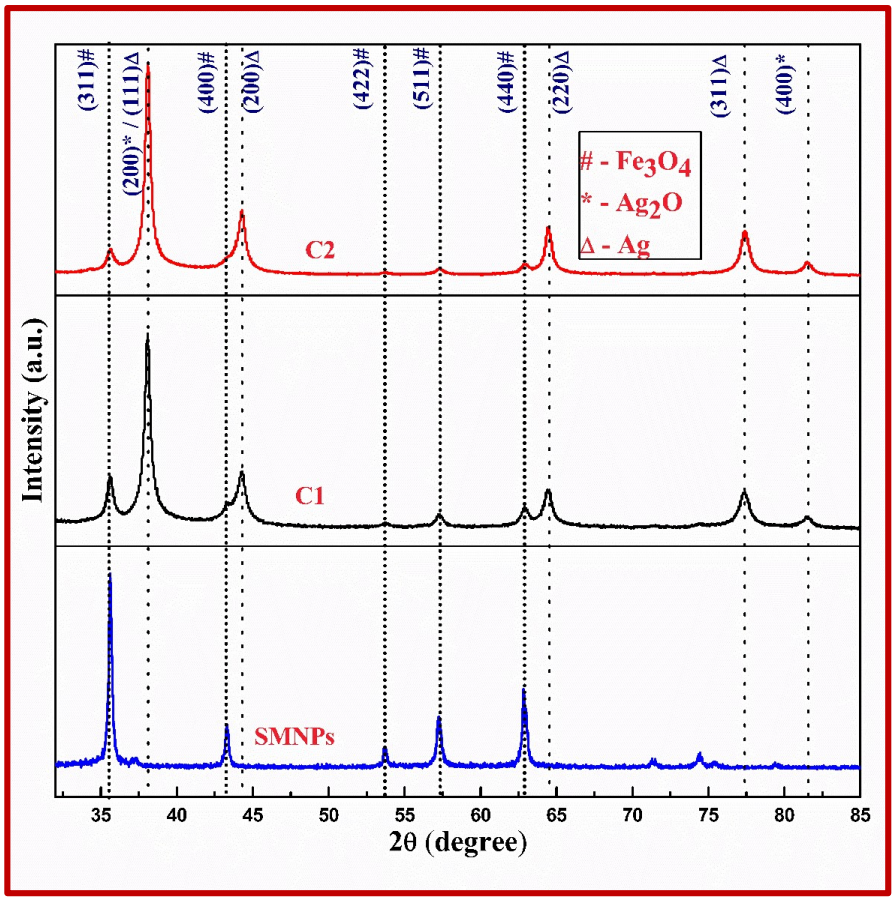

Figure 3.2 X-ray powder diffraction patterns of samples SMNPs, C1 and C2.

Figures 3.3a and 3.3b give the TEM images of samples C1 and C2, respectively. These TEM images show the formation of approximately spherical nanostructures. Figures 3.3c and 3.3d give the nanocomposite particle size distributions of C1 and C2. The average size of the C2 nanoparticles (~22 nm) was larger than those observed in C1 (~19 nm).

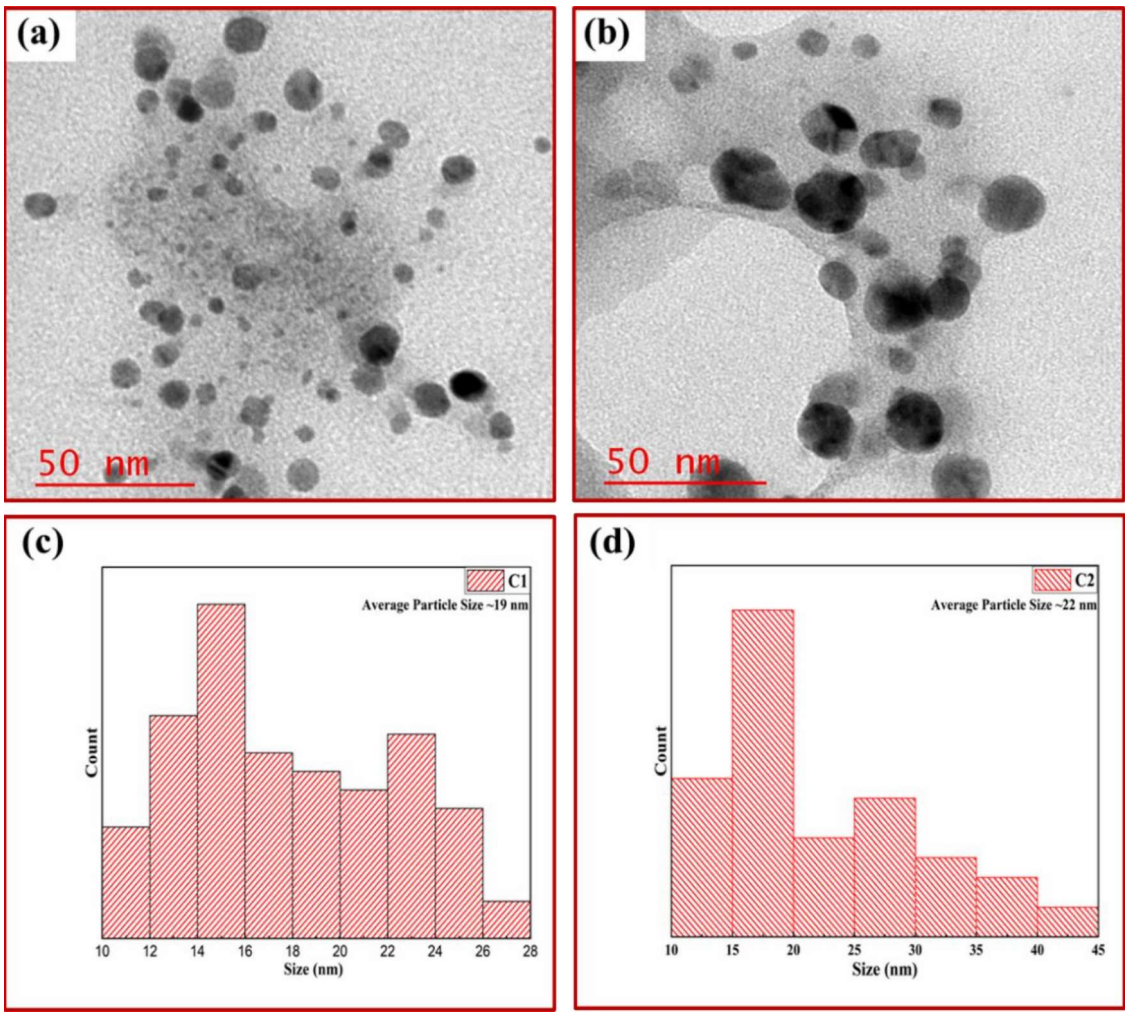

Figure 3.3 TEM images (a, b) and the respective particle size distribution (c, d) of samples C1 and C2.

Figure 3.4 shows a typical HRTEM image of a nanocomposite particle in sample C1. The picture shows two Ag/Ag_2O nanostructures of ~2-4 nm size on the surface of the SMNPs. It is essential to mention that the d-values of the Ag (111) plane and the (200) plane of Ag_2O are quite close. Therefore, it is not possible to distinguish between the two phases. Hence, the nanostructures on top of SMNPs could either be Ag or Ag_2O or both.

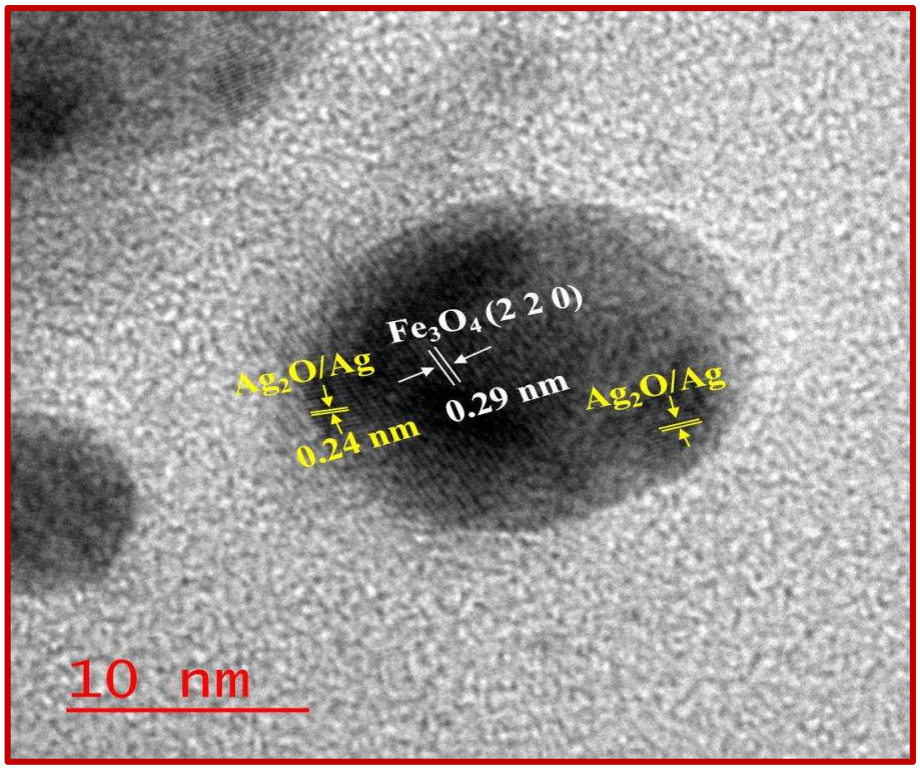

Figure 3.4 HR-TEM micrograph of sample C1 showing Ag/Ag_2O quantum dots formed on SMNPs surface. The part of the manuscript describing the photograph gives the details.

XPS measurements were carried out on samples C1 and C2 to investigate the surface compositions of the nanocomposites prepared. In both samples, the presence of iron was visible, and the Fe 2p peak showed the typical composition for magnetite nanoparticles, consisting of Fe^{2+} and Fe^{3+} species, following the fitting parameters for mixed species of Biesinger and co-workers [Biesinger *et al.* (2011)]. The shifting of visible satellites for Fe^{3+} to higher binding energies indicated the presence of more Fe^{3+} than Fe^{2+}-species, typical for a magnetite modification (2:1 ratio). Anyway, the appearance of Fe signals is an indication that the magnetite core only had a partial cover of silver oxide / elemental silver nanostructures on its surface.

Figure 3.5 gives the XPS results for sample C1 and C2. The survey spectrum analysis shows the presence of carbon, oxygen, silver, and iron in both the samples. The high-resolution spectrum of the O 1s region showed signals for lattice oxides at

529.33 eV as well as for hydroxides, organic oxygen species, and water at 530.71 eV, 532.10 eV, and 533.60 eV, respectively. The signal of lattice oxide showed the presence of silver oxide and iron oxides. Hydroxides formed, because of the alkaline medium, were responsible for 49.81 % of the oxygen species.

A spectrum of the Ag 3d region was measured in high-resolution to investigate the composition of the nanostructures formed on the surface of SMNPs. This spectrum showed two different species of silver. Next to silver (I) oxide at 367.67 eV and 373.67 eV, elemental silver Ag(0) at 368.47 eV and 374.47 eV could be detected, proving the existence of Ag and Ag_2O nanostructures on the surface of SMNPs.

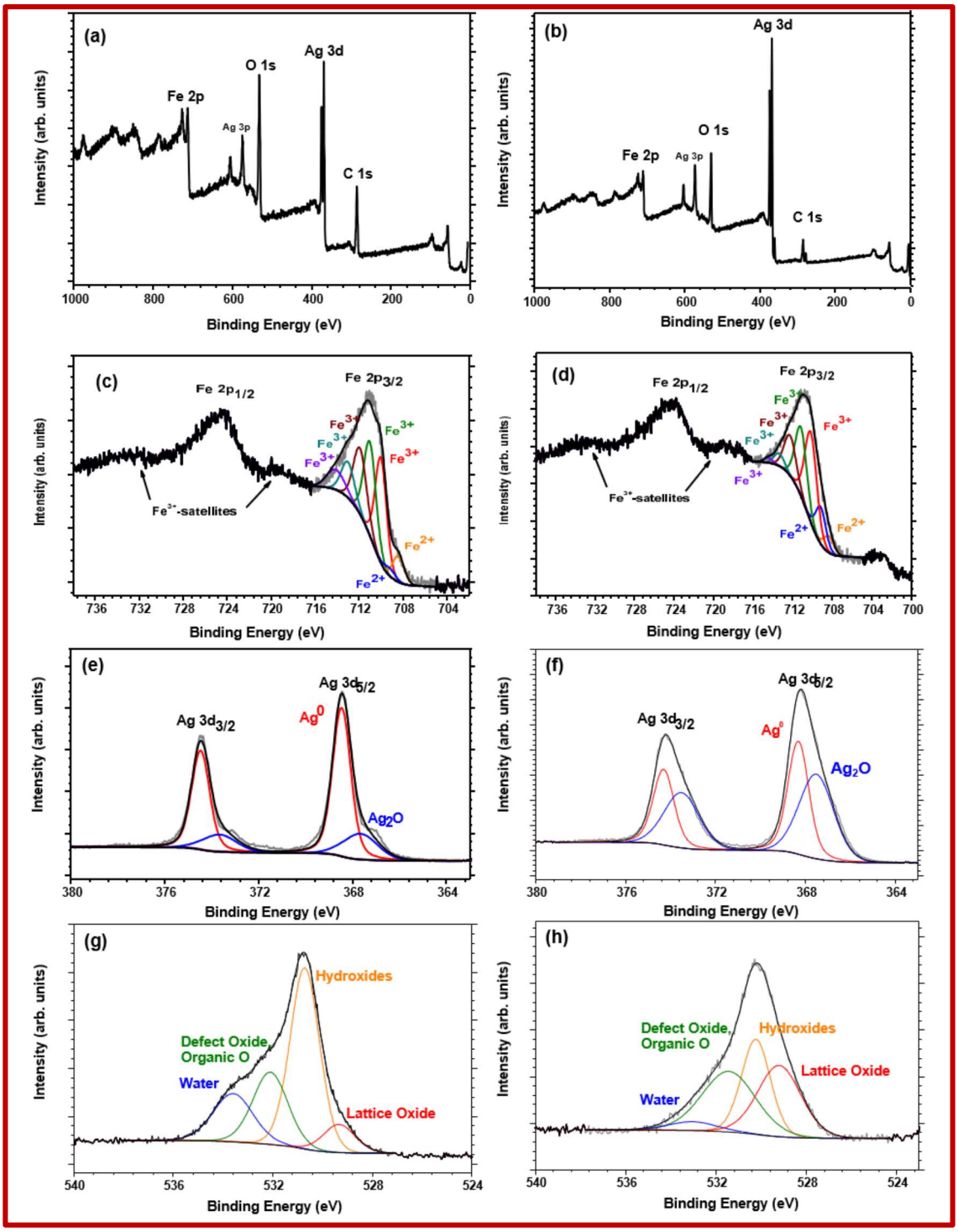

Figure 3.5 XPS analysis of C1 and C2 **(a, b)** survey spectrum **(c, d)** Fe 2p, **(e, f)** Ag 3d, and **(g, h)** O 1s.

The higher concentration of $AgNO_3$ used in the synthesis of C2 led to the formation of the significantly higher amount of Ag or Ag_2O in the nanoparticles of this composite. Despite the higher amount of $AgNO_3$, the O 1s region indicates smaller

amounts of hydroxides on the surface of the sample, but a higher amount of lattice oxide-oxygen. More NaOH reacting with $AgNO_3$ may be resulting in smaller amounts of hydroxides but a higher concentration of Ag_2O on the surface of the sample. Another possibility for the reduced hydroxide peak might be the better coverage of iron oxide with silver/silver oxide. This higher amount of lattice oxide is also evident from the high-resolution measurement of the Ag 3d region. The proportion of 52.56 % silver (I) oxide at 367.52 eV and 373.52 eV in comparison to 47.44 % Ag(0) at 368.31 eV and 374.31 eV is much higher than in sample C1, where it was 22.79 % for Ag(I) and 77.21 % for Ag(0).

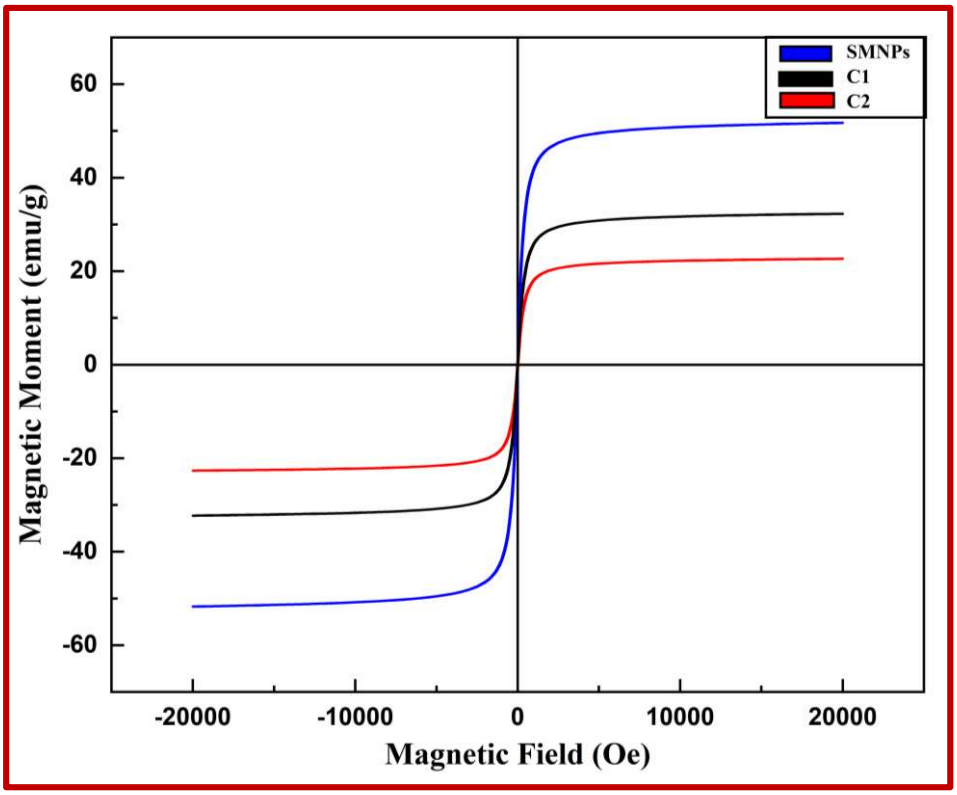

Figure 3.6 Magnetic moment versus magnetic field graph of SMNPs, C1, and C2.

The magnetization curves of SMNPs, C1, and C2 were measured using the Magnetic Property Measurement System (MPMS3)-SQUID VSM. Figure 3.6 displays

magnetization versus magnetic field (M-H loop) plots at room temperature for SMNPs, C1and C2 nanoparticles. Typical superparamagnetic hysteresis characteristics were observed for all three types of nanoparticles investigated. The magnetic moment for SMNPs is the highest. It seems that the magnetic moment decreases with an increase in the size of nanostructures formed on top of the SMNPs [Zhang *et al.* (2016)] due to the shielding effect of the Ag/Ag_2O nanostructures on the magnetization response of the superparamagnetic magnetite core to the external field. Accordingly, the magnetic moment was lowest for the C2 catalyst because of the larger Ag/Ag_2O nanostructures precipitated on the SMNPs. Even after the precipitation of the Ag/Ag_2O nanostructures on the SMNPs, the saturation magnetization values for both C1 and C2 were sufficiently high for the nanoparticles to exhibit easy magnetic recyclability.

Therefore, XPS analysis and HRTEM observations show the formation of the Ag/Ag_2O nanostructures on the SMNPs surfaces. Samples C1 and C2 are made up of different amounts of Ag and Ag_2O phases. The ratio of Ag and Ag_2O phases was about 3:1 in C1, while it was near 1:1 in C2. It appears that the presence of starch molecules on the surface of the precursor SMNPs results in precipitation of discrete Ag/Ag_2O nanostructures. Figure 3.7 displays the schematic model proposed to depict the prepared composite nanoparticles.

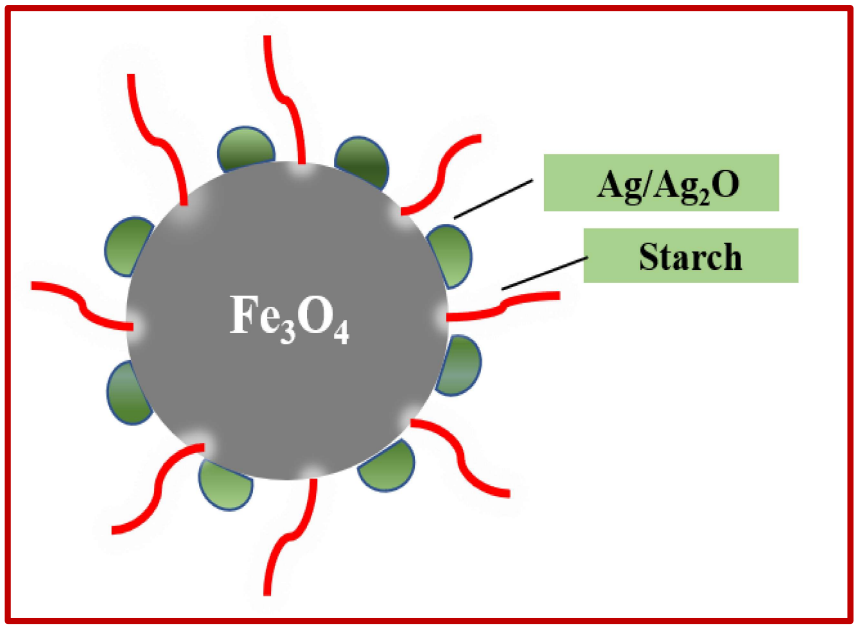

Figure 3.7 Schematic models of possible nanocomposite structures.

The solid-state UV-visible absorption spectra of SMNPs, C1, and C2 were studied to investigate the effect of nanocomposite structural aspects on their band gaps. Tauc plots derived from the UV-visible absorbance data gave the optical band gaps of these samples. Fig. 3.8 shows these plots for SMNPs, C1, and C2. Equation (2.2) gives the Tauc relation between the absorption coefficient alpha (α) and photon energy hυ [Tumuluri *et al.* (2014), Hassanien *et al.* (2015)].

$$\alpha = \left(\frac{\beta}{h\nu}\right)(h\nu - E_g)^n \quad \text{or} \quad (\alpha h\upsilon)^{1/n} = \beta\,(h\nu - E_g) \tag{2.2}$$

In equation (1), α is the molar absorption coefficient, β is a constant called band tailing parameter, and E_g is the allowed energy of the optical bandgap. The exponent n has a value of 1/2 for allowed direct transition and 2 for the allowed indirect transition.

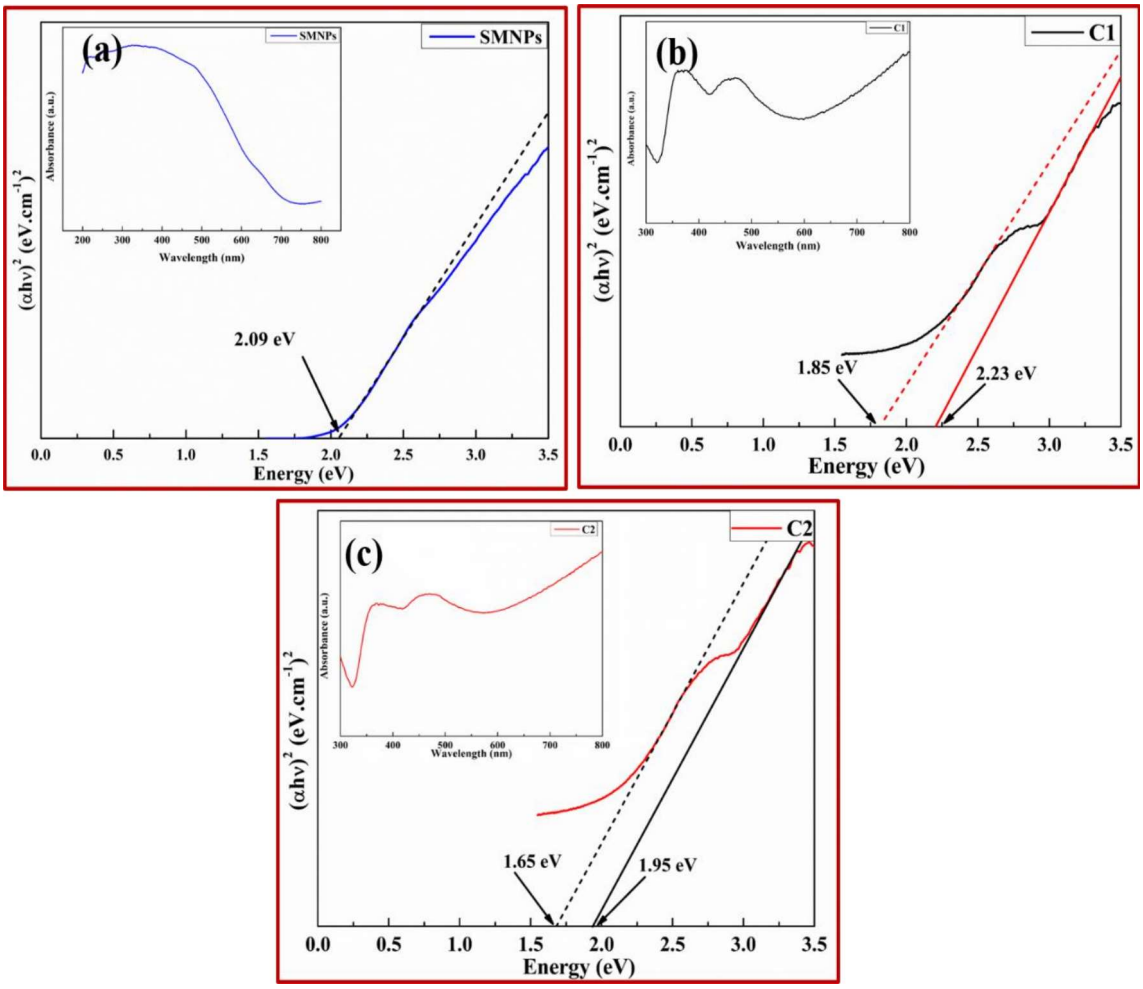

Figure 3.8 Solid-state UV -Vis absorption spectra of **(a)** SMNPs **(b)** C1 and **(c)** C2 nanoparticles and their respective Tauc plots.

The Tauc plot analysis in Fig. 3.8a shows that SMNPs have a direct bandgap of 2.09 eV. In contrast to this, the Tauc plots of samples C1 and C2 display two direct bandgaps (Fig. 3.8b and 3.8c). The bandgap values for the Ag_2O component in C1 and C2 were 1.85 and 1.65eV, respectively. The widening of the bandgap of Ag_2O (from its normal range of 1.2 -1.4eV) was due to the quantum confinement effect of its small particle size. On the other hand, the bandgaps for the starch functionalized magnetite (SM) component in C1 and C2 were 2.23 and 1.95eV, respectively. These were slightly more and lesser than that of the SMNPs alone (~2.1 eV).

Mott–Schottky (MS) plots of SM, Ag_2O, C1, and C2 under dark conditions gave the band edge positions of the two components before and after the nanocomposite formation. Figure 3.9 displays the MS plots of all the samples. SM exhibits a positive slope while Ag_2O has a negative slope, confirming that SM is an n-type, and Ag_2O is a p-type semiconductor. Further, C1 and C2 also show both positive and negative slope parts in their MS plots, implying that these are p-n heterojunction nanocomposites.

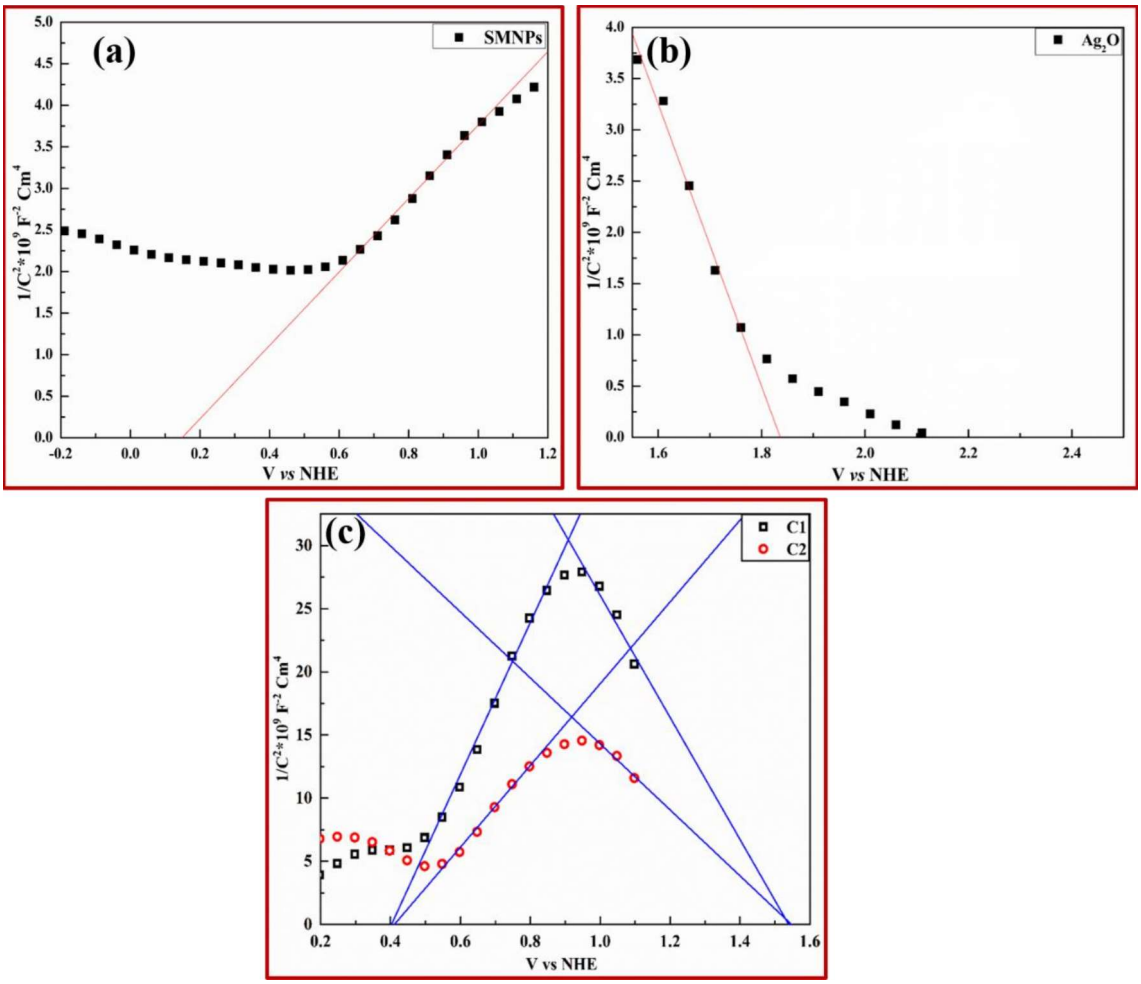

Figure 3.9 Mott Schottky plot of **(a)** SMNPs **(b)**Ag_2O **(c)** C1 and C2 measured under the dark condition in 0.5M Na_2SO_4 at 1 kHz.

Assuming the gap between the flat band potential and the lower edge of CB is negligible for the n-type semiconductor, the CB potential of the n-type semiconductor is

roughly equal to its flat band potential. Similar by assuming the gap between flat band potential and top edge of the VB is negligible for the p-type semiconductor, the VB potential of the p-type semiconductor is equal to its flat band potential. As a result, the CB potential of pure SM component was +0.147 V vs. NHE and VB potential of pure Ag_2O sample was + 1.84 V vs. NHE. After the nanocomposite formation, the CB potential of the SM component shifted to + 0.402 V vs. NHE for C1 and + 0.414 V vs. NHE for C2. Simultaneously, the VB potential of Ag_2O moved to + 1.539 V vs. NHE for C1 and + 1.543 V vs. NHE for C2. Note that the CB values of the SM part of C1 and C2 are almost the same. Similarly, the VB levels of the Ag_2O components of C1 and C2 are also very similar. In all measurements, the potential vs. Ag/AgCl reference electrode is converted to the potential vs. NHE by the relation $V(NHE) = V(Ag/AgCl) + 0.059\,pH + 0.197$ (here $pH = 7$). Thus, after the p-n junction formation, the CB potential of the SM component and VB potential of the Ag_2O part shift to equilibrate the Fermi level [Tang *et al.* (2019)]. Figure 3.10 illustrates the band alignments found for the SM and Ag_2O components before and after the Fermi level equilibrium.

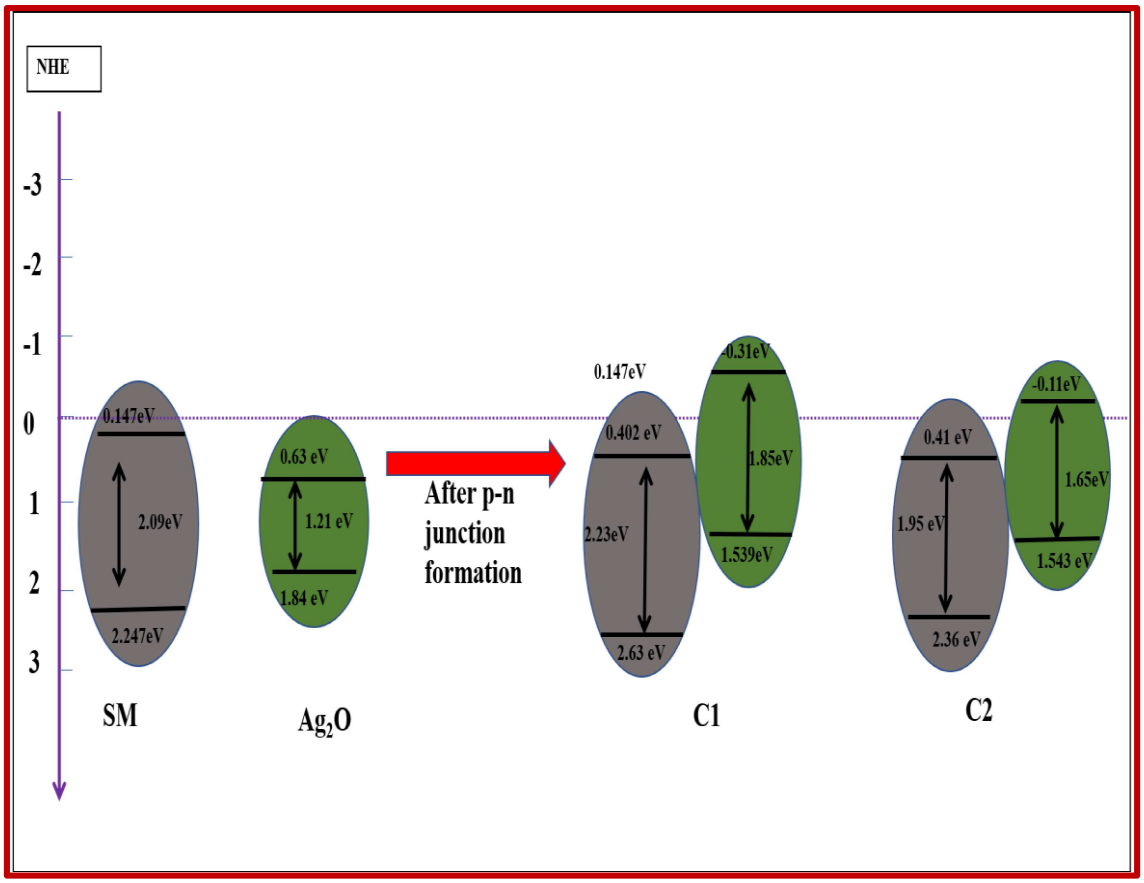

Figure 3.10 Band edges and band gap values of the semiconducting components constituting C1 and C2.

Figure 3.11 gives the Nyquist plots of electrochemical impedance spectroscopy (EIS) for C1 and C2 for the investigation of the electron transfer kinetics of the catalysts. The smaller diameter of the semicircle implies a lower charge transfer resistance at the electrode/electrolyte surface [Wu *et al.* (2019), Wang *et al.* (2019a), Li *et al.* (2019), Wang *et al.* (2019b)]. Therefore, sample C1 shows more efficient electron-hole separation, which is consistent with the higher Ag amount in its composition. The Ag metal part could be facilitating better electron conduction between the two semiconducting components or acting as a co-catalyst.

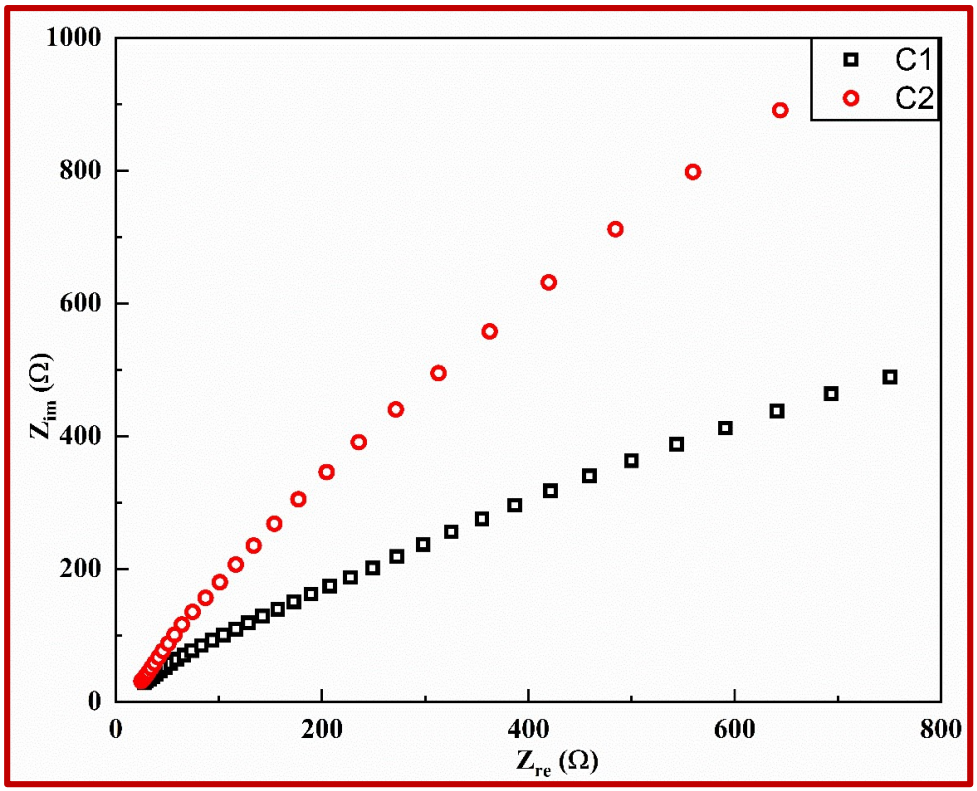

Figure 3.11 Nyquist plot of EIS spectra for C1 and C2.

3.3.2 Catalytic activity

3.3.2.1 Photocatalytic production of H_2O_2

Experiments at different pH-values showed that acidic pH (~2) conditions provided the best H_2O_2 formation results. Figure 3.12 presents the effect of pH on the production of H_2O_2. The increase in pH to 6.5 resulted in a decrease in H_2O_2 production. H_2O_2 production is a pH-dependent process because it takes place by a proton-coupled electron transfer (PCET) mechanism [Thakur *et al.* (2017)]. Thus, reduction of pH facilitated oxygen reduction to hydrogen peroxide ($O_2 + 2H^+ + 2e^- \rightarrow H_2O_2$).

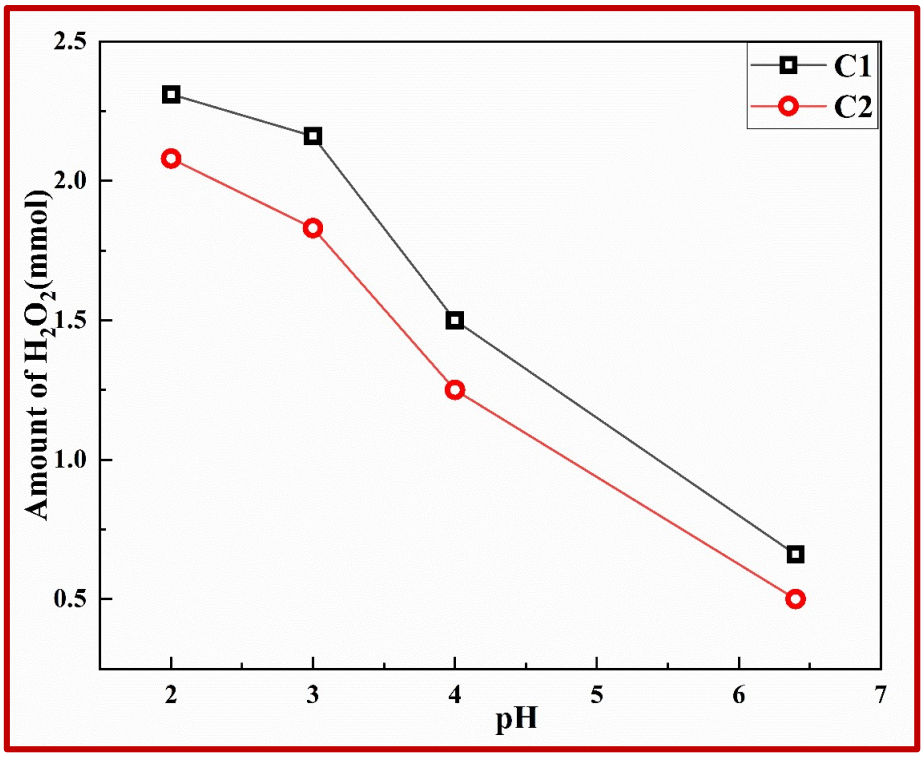

Figure 3.12 H_2O_2 production per gram of catalyst in one hour at different pH-values.

3.3.2.2 Catalyst Recyclability

Figure 3.13 displays the reusability experiments results of catalysts C1 and C2 for the production of H_2O_2. The duration of each experiment (at pH 3) was one hour. We performed ten cycles to test the reusability of the catalyst. Both catalysts exhibit recyclability with almost equal efficiencies. After the sixth run, H_2O_2 production becomes almost constant (~60-65%).

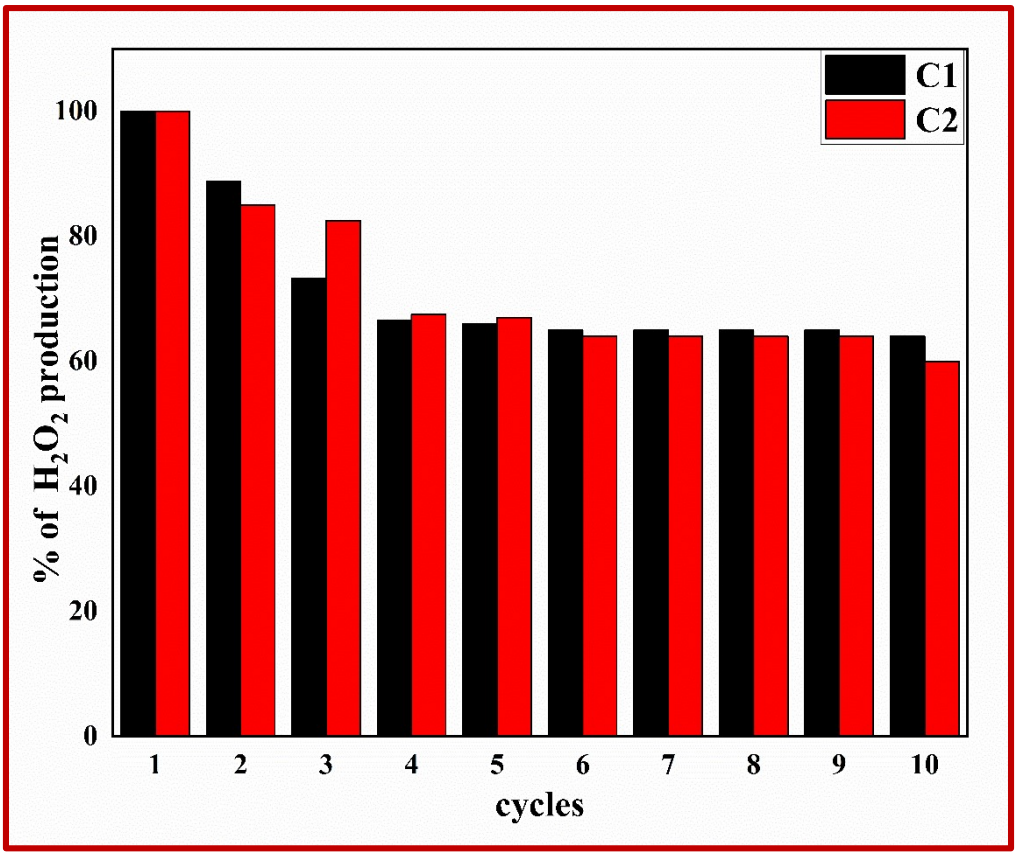

Figure 3.13 Ten cycles C1 and C2 reusability results in histogram format for H_2O_2 production.

3.3.2.3 H_2O_2 production in the presence of an electron donor

As mentioned earlier, photocatalytic H_2O_2 production reactions are generally carried out by light irradiation of O_2-saturated water with a photocatalyst in the presence of an electron donor such as alcohol, oxalic acid, etc. [Zuot *et al.* (1992), Shiraishi *et al.* (2015)]. In contrast to this, the photocatalysts in the present investigation demonstrated H_2O_2 production at a significant rate from only water and dissolved oxygen. For the sake of comparison, photocatalytic experiments were also carried out in the presence of KI and isopropyl alcohol (i-PA) to understand whether these electron donor molecules can further enhance the rate of H_2O_2 production. While KI is well known as an electron donor or hole scavenger, i-PA can also act as an efficient organic electron donor for the

production of H_2O_2 [Wang *et al.* (2014), Zhang *et al.* (2012)]. The addition of these two electron donors reinforces to improve the photocatalytic production of H_2O_2 significantly. Table 3.1 compares H_2O_2 output (after one hour to exposure to visible light) values using the investigated photocatalysts under different conditions. A significant (~60-80%) increase in H_2O_2 formation occurred in the presence of electron donors such as i-PA and KI. However, even in the absence of electron donors, the H_2O_2 production was substantial. Furthermore, these values are definitely among the best reported to date in the literature [Shiraishi *et al.* (2014), Zhang *et al.* (2016), Thakur *et al.* (2017)].

Table 3.1 Visible light photocatalytic H_2O_2 production at pH 3 (under different reaction conditions.

System	H_2O_2 amount (in millimoles) per gram of catalyst	
	C1	C2
Water + Catalyst	2.16	1.83
Water + Catalyst + KI	3.00	3.00
Water + Catalyst + i-PA	3.16	3.33

3.3.2.4 H_2O_2 production in different controlled conditions

Several control experiments were carried out in various situations to investigate the mechanism of H_2O_2 production. The first control experiment was done with acetonitrile as the solvent instead of water, along with O_2 purging. The rest of the parameters (catalyst amount, etc.) were unchanged. No H_2O_2 production was detected under these conditions, leading to the conclusion that H_2O_2 production proceeded by water oxidation [Kofuji *et al.* (2018)]. Additionally, this also confirmed that no impurities or catalyst

decomposition was involved. The second control experiment investigated the absence of O_2 on H_2O_2 production under continuous Ar purging. H_2O_2 production dropped to negligible levels, confirming that O_2 reduction was responsible for it [Hou *et al.* (2017)]. Another control experiment was on an aqueous solution with saturated oxygen, keeping the rest of the experimental parameters the same. Continuous O_2 purging of the reaction mixture was done in this control experiment. H_2O_2 production rate remained the same under these conditions, indicating that O_2 reduction was not the rate-limiting step for the catalysts studied in the present investigation [Kofuji *et al.* (2018), Hirakawa *et al.* (2016), Kofuji *et al.* (2017)].

3.3.3 Mechanism of photocatalytic H_2O_2 production

The prepared nanocomposites consisted of small, and discrete Ag/Ag_2O nanostructures precipitated on the SMNPs. Furthermore, both SM and Ag/Ag_2O components have band gaps in the visible range. The collected experimental evidence suggests the following mechanism (Figure 3.14) for the generation of H_2O_2 from an aqueous suspension of s-$Fe_3O_4/Ag/Ag_2O$ under visible light irradiation.

Both components were exposed to visible light irradiation and got photo-excited. As mentioned earlier, (in C1 and C2) SM and the Ag_2O formed a p-n heterojunction, which shifted the VB of the SM component to a more positive (or lower) position. The improved VB position of the SM component resulted in a better driving force for water oxidation.

Charge separation can take place in two ways. First, by electron transfer from the CB of the photo-excited p-type Ag_2O to the CB of the SM component. Secondly, the electrons excited to the CB of the SM component migrate to the Ag part. Plasmonic absorbance stimulates the electron pool in Ag to generate hot electrons with enough

energy to reduce oxygen through a 2-electron mechanism [Liu *et al.* (2018)]. Here, it is essential to note that the lower CB positions of the SM component forbid a single electron oxygen reduction pathway. Furthermore, being plasmonic Ag must also be capturing and re-radiating visible light for more efficient photocatalysis.

The photocatalytic formation of H_2O_2 from only water and oxygen has two parts. The first step is water oxidation to generate oxygen. The requirement for this is that VB of the photocatalyst should be more positive than 1.23eV. Subsequently, the two-electron reduction of oxygen results in the formation of H_2O_2. The redox potential of this step is +0.68eV. For efficient reduction, the CB of the photocatalyst should have a value lesser than +0.68 eV.

In the photocatalyst designed in the present investigation, the VB of the SM component is ~2.63 eV for C1 and ~2.36 eV for C2. While both satisfy the criterion for water oxidation, the VB of C1 demonstrates a better driving force. Similarly, the CB of C1 and C2 are ~0.4 eV, which also satisfies the potential requirement for 2-electron oxygen reduction criteria. But an increase in H_2O_2 production with the Ag percentage indicates that the 2-electron oxygen reduction occurred on this component. Therefore, the electrons on the CB of the SM component migrate to the Ag part. As mentioned earlier, many examples in literature show plasmonic excitation of the electron pool in Ag generates hot electrons with enough driving force (concerning potential) to reduce oxygen through a 2-electron mechanism [Liu et al (2018)]. Consequently, oxygen reduction to H_2O_2 occurred on the Ag part, while water oxidation mainly took place on the SM component. Note that there are quite a few references that have also investigated and reported suitable oxygen reduction properties of various magnetite nanocomposites [Zhou *et al.* (2018), Karunagaran *et al.* (2013), Abdullah *et al.* (2020)]. However, the

fact that C1 demonstrates better H_2O_2 formation indicates that two-electron oxygen reduction mainly took place by the co-catalytic activity of Ag.

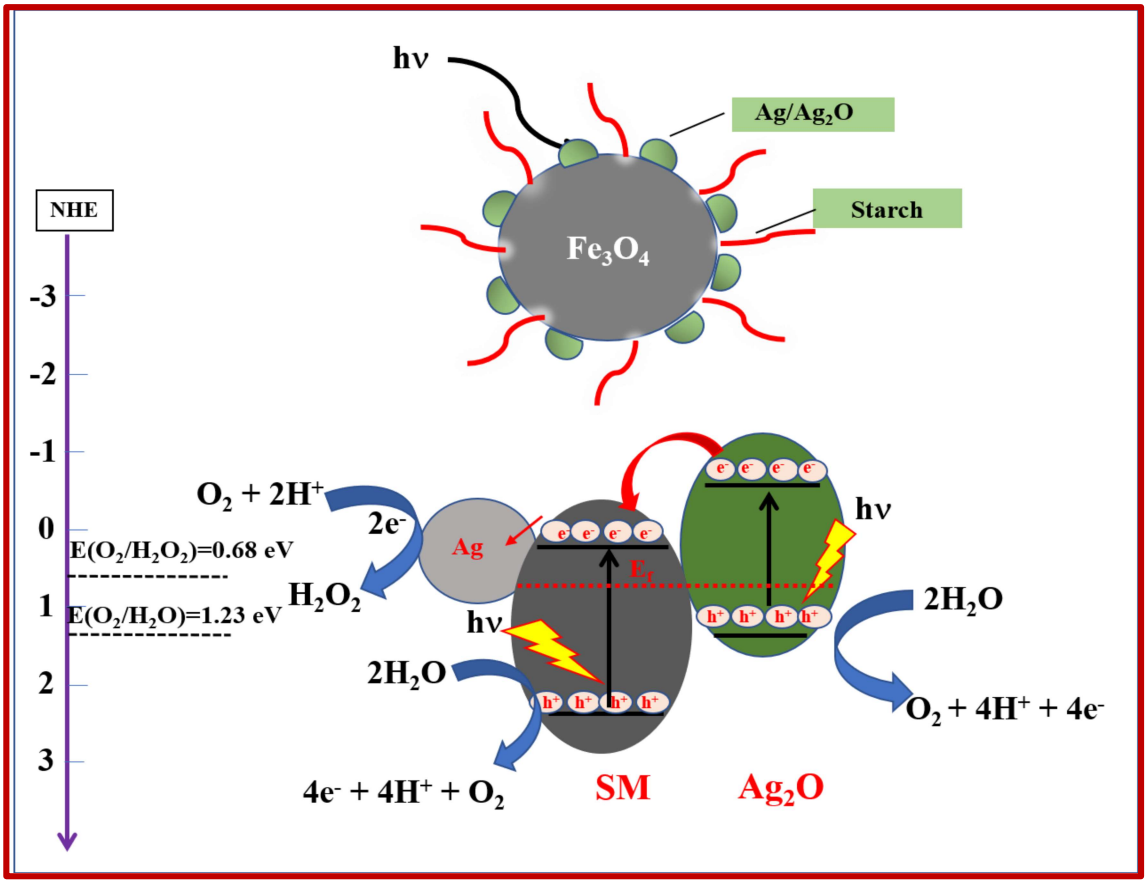

Figure 3.14 Schematic representation of the proposed mechanism.

3.4 Conclusions

Highly efficient production of H_2O_2 takes place on the nanocomposites with Ag/Ag_2O fine nanostructures precipitated on starch functionalized superparamagnetic magnetite nanoparticles under visible light conditions from only water and air as reactants. Photocatalytic production of 2.16 millimoles of H_2O_2 at pH 2 was achieved in one hour without organic electron donors. In the presence of electron donors, the formation of H_2O_2 increased to more than 3 millimoles per hour.

These photocatalysts were prepared by a two-stage co-precipitation protocol that successfully limited the size of nanostructures of Ag/Ag_2O to within the quantum confinement regime. Consequently, the bandgap of Ag_2O increased from 1.2-1.4 eV range to the 1.65 – 1.85 eV range. Starch functionalized magnetite (SM) and Ag_2O components were found to have staggered band alignment but form a p-n heterojunction. On irradiation by visible light, electrons were excited both in SM and Ag_2O parts. Charge separation occurred by the transfer of electrons to the CB of the SM component and then to the Ag part of the nanocomposites. Oxygen reduction to produce H_2O_2 occurred at the Ag co-catalyst, while water oxidation mainly takes place on lower VB of the SM component. The fact that H_2O_2 production increases with the percentage of metallic Ag reinforce this suggestion that oxygen reduction occurs on the Ag part of the nanocomposite. Thus, fine Ag nanostructures on the SM could be acting as co-catalysts to reduce oxygen by the two-electron pathway through the plasmonic hot-electron formation. On the other hand, the LSPR of the Ag component could be making the re-emission of visible light possible, resulting in better photo-efficiency. Superparamagnetic properties of these photocatalysts facilitate easy recyclability for H_2O_2 production.